A Composite Cell-Multiresolution Time-Domain Technique for the Design of Antenna Systems Including Electromagnetic Band Gap and Via-Array Structures

Nathan Bushyager, *Student Member, IEEE*, John Papapolymerou, *Senior Member, IEEE* and Manos M. Tentzeris, *Senior Member, IEEE*

***Abstract*— In this paper the Haar-wavelet multiresolution time-domain (MRTD) scheme is modified in a way that enables the modeling of arbitrarily positioned metals within a cell, leading to the development of composite cells that are useful for the simulation of highly detailed structures. The technique is applied through the use of wavelet reconstruction and deconstruction matrices to explicitly set field values at PEC interfaces. Using this scheme, MRTD can be used to drastically reduce the number of cells needed to simulate complex antenna geometries including RF-MEMS, EBGs, and via arrays, while taking full advantage of the technique's inherent time- and space-adaptive gridding.**

***Index Terms*— FDTD method, wavelet transforms, MRTD method, Haar transforms, time-domain techniques, multiresolution analysis, EBG structures, SHS, via-array structures, antenna systems**

I. Introduction

Current demands on commercial communications devices are requiring the integration of antennas and supporting devices, such as baluns and filters, into packages along with microwave components. This integration creates challenges in shielding sensitive components from radiation and surface waves caused by other elements in close proximity. This has led to the use of a number of techniques, including electronic band gap (EBG) [1], soft-and-hard-surface (SHS) [2], and metamaterials [3]. These structures are difficult to characterize without full-wave simulation, however, the size and complexity of these structures often pushes the limits of existing techniques.

The simulation of these complex devices requires the use of extremely small elements or cells, which can tax many simulation tools beyond their limits. This has led to the use of a combination of methods, such as full-wave simulation and microwave circuit simulation, or, if higher accuracy is required, the use of a parallel full-wave simulator on specialized hardware. In order to achieve realistic simulation times, methods that are more efficient but of similar accuracy are necessary.

One common tool used in the simulation of microwave devices is the finite-difference time-domain (FDTD) technique [4]. FDTD has the advantage that it is both simple to code and versatile enough to model a variety of structures and materials. In addition, the FDTD method parallelizes easily and can be used to simulate structures requiring a large number of cells. However, the FDTD method has limitations, one of which is its grid requirements. Methods exist to use a non-uniform [5] or subcell [6] grid in FDTD; however, these techniques can be difficult to apply, impose stability conditions, and are fixed throughout simulation. In addition, FDTD requires the use of a small spatial and time step in order to keep the grid numerical dispersion low. One technique that has been developed to combat these limitations is the multiresolution time-domain (MRTD) technique [7].

MRTD uses a wavelet expansion of electromagnetic fields to generate a scheme that has an inherent adaptive grid. In addition, depending on the chosen wavelet basis, a numerical dispersion superior to that of FDTD can be achieved [8-11]. The wavelets used in the Haar-based MRTD method are derived from pulses, the basis used in the FDTD method. The advantage of Haar MRTD over FDTD is its inherent capability of time- and space- adaptive gridding. However, the method cannot be effectively applied to complex structures because of the difficulty in representing hard boundaries.

Due to the use of wavelets, the Haar MRTD cell size is equivalent to that of several FDTD cells. In FDTD, a perfect electrical conductor (PEC) boundary condition can be applied in a cell by zeroing out the electric field that is tangential to the PEC surface. In Haar MRTD, zeroing out fields at a single point is more difficult because the field values are not represented by only one coefficient, but rather with a sum of many scaling and wavelet coefficients. This difficulty has limited the application of MRTD because PEC structures need

Manuscript received Febuary 6, 2003. This work was supported in part by the Georgia Tech NSF Packaging Research Center, The Georgia Electronic Design Center, and NSF CAREER Grant# 9984761.

The authors are with The Georgia Electronic Design Center, The Georgia Institute of Technology, (404-385-0378; fax: 404-894-0222; e-mail: nbushyager@ece.gatech.edu, papapol@ece.gatech.edu, etentze@ece.gatech.edu).

to be modeled using entire Haar cells, where all of the coefficients within a cell have to be zeroed to represent the PEC boundary condition. This significantly reduces the computational benefits from the inherent adaptive gridding in the MRTD method, and imposes a maximum size on the MRTD cells of the smallest feature in the simulated structure.

In this paper, a method is presented in which the PEC boundary condition can be applied to any intracell arrangement of Haar MRTD equivalent grid points. Previous methods have focused on the use of image theory [12], this method utilizes a wavelet decomposition/reconstruction technique. This technique allows full advantage to be taken of the time- and space-adaptive gridding of the MRTD technique. Due to the fact that PEC structures can be represented within cells, the adaptive resolution of the grid can be increased in areas of the grid with fine geometrical details and field variations. Elsewhere, high-resolution wavelets can be suppressed leading to a very coarse grid. Using this technique, it is possible to model complex structures with significantly fewer grid points than required in FDTD and previous MRTD approaches.

II. MRTD Background

The multiresolution time-domain technique (MRTD) is the result of the application of the method of moments to Maxwell's time-domain curl equations using scaling and wavelet basis functions in space [7-14]. The choice of a wavelet basis determines the properties of the simulator and often reduces the numerical dispersion that is associated with the FDTD method [8-12]. The other major advantage of wavelet analysis in electromagnetics is the ability of wavelets to represent increasingly higher frequency content as their resolution is raised [7]. The number of wavelets used in a field representation can be varied as a function of time and space, and thus a simulator using this method can adapt to simulate complex field interaction using minimal computational resources.

The method presented in this paper is based on the use of Haar scaling and wavelet functions in space and only Haar scaling functions (pulses) in time [14]. The pulse derived basis functions used in this method do not provide better numerical dispersion than that of FDTD [15]. The advantage of using Haar wavelets is that they provide a natural framework for adaptive resolution, while avoiding instabilities inherent in some FDTD-based subgridding approaches. In addition, this gridding can vary not only as a function of space, but also as a function of time. The resulting Haar cells can be significantly larger than their FDTD counterparts because they contain many equivalent FDTD grid points due to the use of multiple coefficients per cell. The use of this technique has been limited, however, because of the difficulty of representing fine yet electrically significant details in these grids.

In FDTD, perfect electrical conductors (PECs) are represented by zeroing tangential electric field components. In MRTD, no such direct application exists, because the directly computed values are scaling and wavelet coefficients, not total field values. The actual field values can be determined only through field reconstruction.

III. MRTD Formulation

In the following sections, a method to model PECs at arbitrary intracell grid points is presented. The following derivation is based on a 2D Haar scaling and wavelet spatial expansion, although the same approach can be applied in 3D (or 1D) with minor changes. The TE_z mode equations in two dimensions are given by

$$\frac{\partial E_x}{\partial t} = \frac{1}{\varepsilon}\frac{\partial H_z}{\partial y} \tag{1}$$

$$\frac{\partial E_y}{\partial t} = -\frac{1}{\varepsilon}\frac{\partial H_z}{\partial x} \tag{2}$$

$$\frac{\partial H_z}{\partial t} = \frac{1}{\mu}\left[\frac{\partial E_x}{\partial y} - \frac{\partial E_y}{\partial x}\right] \tag{3}$$

In these equations, source and loss terms are omitted for simplicity. Furthermore, ε and μ are assumed to be constant throughout each MRTD cell. These conditions are not required, and the proposed subcell technique is perfectly compatible with a scheme that includes these features. Their elimination simply allows the following sections to focus on the new technique.

The first step in deriving the MRTD update equations is to expand the E and H fields into scaling and wavelet functions in space and pulses in time. The scaling function and r=0 wavelet for the Haar scheme are presented in Fig. 1. The wavelet has the same domain as the scaling function, but is valued +1 in the first half of the domain and -1 in the second half. By choosing the appropriate weights for these two functions, their sum can be made to match arbitrary values on both halves of the domain. Fig. 2 shows the wavelets for r=1 and r=2. For each level of I, the number of wavelet coefficients per level is doubled, while the domain of each wavelet is halved. In addition, the magnitude of the function is $2^{r/2}$, in order to guarantee the orthonormalization of the expansion basis (the inner product of any function with itself is one). Two dimensional functions can be generated by placing the scaling and wavelet functions along each axis and considering all combinations that can be obtained by multiplying each function on one axis by every function on the other. For example, the four two dimensional functions that are generated by using the scaling function and the r=0 wavelet in each direction are presented in Fig. 3.

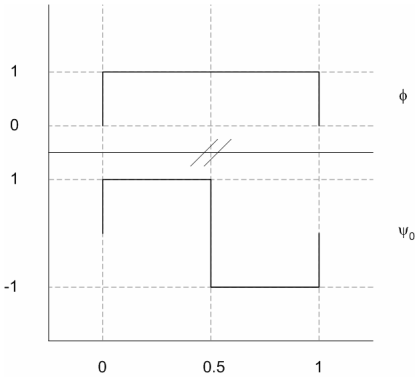

Fig. 1 Haar scaling function and r=0 wavelet

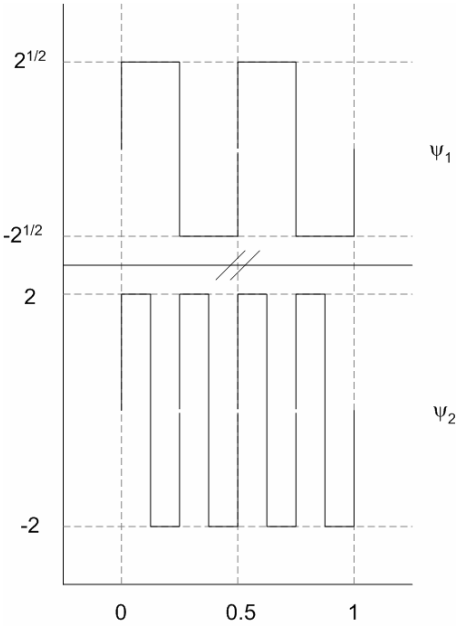

Fig. 2 Haar wavelet functions for r=1,2

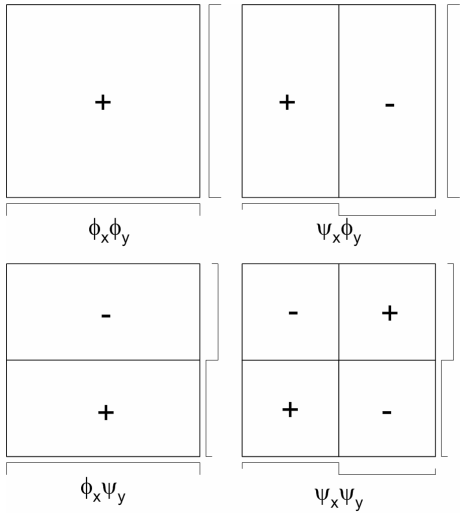

Fig. 3 Coefficients for 2D field representation with rmax=0

Using a 2D Haar expansion,

$$E_x(x) = \sum_{n,i,j} h_{n(t)} \left[\begin{array}{l} {}_n E_{i,j}^{x,\phi\phi} \varphi_i(x)\varphi_j(y) + \\ \sum_{r=0}^{r_{\max}} \sum_{p=0}^{2^r-1} {}_n E_{i,j,r,p}^{x,\psi\phi} \psi_{i,p}^r(x)\varphi_j(y) + \\ \sum_{r=0}^{r_{\max}} \sum_{p=0}^{2^r-1} {}_n E_{i,j,r,p}^{x,\phi\psi} \varphi_i(x)\psi_{j,p}^r(y) + \\ \sum_{r=0}^{r_{\max}} \sum_{p=0}^{2^r-1} \sum_{s=0}^{r_{\max}} \sum_{q=0}^{2^s-1} {}_n E_{i,j,r,p,s,q}^{x,\psi\psi} \psi_{i,p}^r(x)\psi_{j,q}^s(y) \end{array} \right] \quad (4)$$

following the notation in [7]. In this case $\varphi_i(x) = \varphi\left(\frac{x}{\Delta x} - i\right)$ and $\psi_{i,p}^r(x) = 2^{r/2}\psi_0\left(2^{r/2}\left(\frac{x}{\Delta x} - i\right) - p\right)$. The maximum level of wavelet resolution is r_{max}. The four groups of terms in the above equation represent the product of the *x*- and *y*- oriented wavelet expansions. The terms are the *x*-scaling/*y*-scaling, *x*-wavelet/*y*-scaling, *x*-scaling/*y*-wavelet, and *x*-wavelet/y-wavelet terms, respectively. In each cell, represented by (*i,j*) in 2D, there is a set of $2^{D(r_{\max}+1)}$ coefficients, where D is the dimension of the simulator ($2^{2(r_{\max}+1)}$ in the 2D case). Neglecting the wavelet terms yields an FDTD field expansion, while using a maximum wavelet resolution of r_{max}=0 leads to four coefficients per cell. The wavelet coefficients for the r_{max}=0 case are presented in Fig. 3. In this case it can be seen that these wavelets add, or reconstruct, to four independent (equivalent grid point) values. In Haar MRTD schemes, the number of these points is always equal to the number of coefficients used to represent the field. These points are located at 1/4 and 3/4 of the domain of the highest resolution wavelets as shown in Fig. 4. The coordinate system of Fig. 4 will be used to refer to these individual points in the rest of the paper.

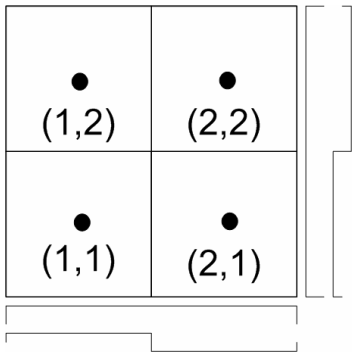

Fig. 4 Equivalent grid points of 2D MRTD cell with r_{max}=0

Similar expansions can also be performed for the other field components. It was noted in [14,15] that an offset of $1/2^{r_{\max}+2}$ leads to a true doubling of resolution for each increase in r_{max}, and dispersion performance equivalent to an FDTD grid that has cell spacings of the MRTD equivalent grid points. In the case shown above, the H_z fields are offset from the E_x fields by $1/2^{r_{\max}+2}$ in the y direction and the E_y fields by $1/2^{r_{\max}+2}$ in both the x and y directions. This offset, shown in Fig. 5 for r_{max}=0, arranges the equivalent grid points in the same fashion

as the Yee leapfrog scheme [4,15].

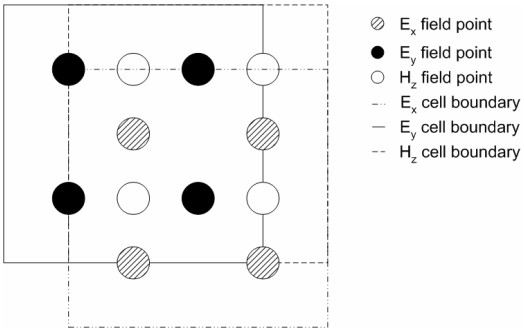

Fig. 5 MRTD cell for rmax=0 showing Yee cell field arrangement

To determine the MRTD update equations, the wavelet expansions of the fields are inserted into Maxwell's equations and the method of moments is applied. For ease of presentation, and to illustrate the subcell method presented in the next section, the field expansion coefficients are presented in a similar method as in [14], as vectors of all coefficients within a cell. For example,

$$ {}_{n}\mathbf{E}^{\mathbf{x}}_{\mathbf{i,j}} = \begin{bmatrix} {}_{n}E^{x,\phi\phi}_{i,j} \\ {}_{n}E^{x,\psi\phi}_{i,j} \\ {}_{n}E^{x,\phi\psi}_{i,j} \\ {}_{n}E^{x,\psi\psi}_{i,j} \end{bmatrix} \tag{5} $$

is the vector of the E_x coefficients for each cell in the r_{max}=0 case. When the MRTD update equations (6)-(8) are presented in this fashion, they appear very similar to their FDTD analogues:

$$ {}_{n}\mathbf{E}^{\mathbf{x}}_{\mathbf{i,j}} = {}_{n-1}\mathbf{E}^{\mathbf{x}}_{\mathbf{i,j}} + \frac{\Delta t}{\varepsilon \Delta y}\mathbf{U}_{\mathbf{E_x}} \begin{bmatrix} {}_{n-1}\mathbf{H}^{\mathbf{z}}_{\mathbf{i,j}} \\ {}_{n-1}\mathbf{H}^{\mathbf{z}}_{\mathbf{i,j-1}} \end{bmatrix} \tag{6} $$

$$ {}_{n}\mathbf{E}^{\mathbf{y}}_{\mathbf{i,j}} = {}_{n-1}\mathbf{E}^{\mathbf{y}}_{\mathbf{i,j}} - \frac{\Delta t}{\varepsilon \Delta x}\mathbf{U}_{\mathbf{E_y}} \begin{bmatrix} {}_{n-1}\mathbf{H}^{\mathbf{z}}_{\mathbf{i,j}} \\ {}_{n-1}\mathbf{H}^{\mathbf{z}}_{\mathbf{i-1,j}} \end{bmatrix} \tag{7} $$

$$ {}_{n}\mathbf{H}^{\mathbf{z}}_{\mathbf{i,j}} = {}_{n-1}\mathbf{H}^{\mathbf{z}}_{\mathbf{i,j}} + \frac{\Delta t}{\mu} \left(\frac{1}{\Delta y}\mathbf{U}_{\mathbf{H_{Ex}}} \begin{bmatrix} {}_{n-1}\mathbf{E}^{\mathbf{x}}_{\mathbf{i,j}} \\ {}_{n-1}\mathbf{E}^{\mathbf{x}}_{\mathbf{i,j+1}} \end{bmatrix} - \frac{1}{\Delta x}\mathbf{U}_{\mathbf{H_{Ey}}} \begin{bmatrix} {}_{n-1}\mathbf{E}^{\mathbf{y}}_{\mathbf{i,j}} \\ {}_{n-1}\mathbf{E}^{\mathbf{y}}_{\mathbf{i+1,j}} \end{bmatrix} \right) \tag{8} $$

The matrices **U** represent the inner products between the testing wavelet and scaling functions and the derivatives of these functions that are obtained by inserting the scaling/wavelet expansion into Maxwell's equations. Δx and Δy are the dimensions of the MRTD cell. When the inner products are determined, the only non-zero results come from the nearest neighbor of each cell. Thus, for the update of each point, only the coefficients from the surrounding fields are required. The stacked vector notation of (6)-(8) of the field vectors multiplied with the U matrices represents a single vector; the vectors consist of the field coefficients from the first cell required for the update, followed by the coefficients of the second cell. As there are $2^{2(r_{\max}+1)}$ coefficients per cell, the U matrix is $2^{2(r_{\max}+1)}$ by $2^{2(r_{\max}+1)}$. An example is:

$$ \mathbf{U}_{\mathbf{H_{Ey}}}(r_{\max}=0) = \begin{bmatrix} -1 & -1 & 0 & 0 & 1 & 1 & 0 & 0 \\ 1 & -3 & 0 & 0 & -1 & -1 & 0 & 0 \\ 0 & 0 & -1 & -1 & 0 & 0 & 1 & 1 \\ 0 & 0 & 1 & -3 & 0 & 0 & -1 & -1 \end{bmatrix} \tag{9} $$

The update equations (6)-(8) can be used in a time loop in a method analogous to FDTD. The time step,

$$ \Delta t = \frac{1}{c\sqrt{\left(\frac{2^{r_{\max}+1}}{\Delta x}\right)^2 + \left(\frac{2^{r_{\max}+1}}{\Delta y}\right)^2}} \tag{10} $$

is equal to the time step in FDTD for a cell with the same dimensions as the MRTD equivalent cell.

In order to use the information contained in the wavelet field representation, the values of the fields must be reconstructed at the equivalent grid points by summing the value of all scaling and wavelet coefficients at these points. Using similar vector notation to that used in the update equations,

$$ \mathbf{F_R} = \mathbf{R}\mathbf{F_W} \tag{11} $$

gives the reconstructed field values at each equivalent grid point in a cell. $\mathbf{F_r}$ represents the reconstructed E or H fields and $\mathbf{F_w}$ represents the scaling/wavelet decomposition of the fields. **R** is the square $2^{2(r_{\max}+1)}$ by $2^{2(r_{\max}+1)}$ reconstruction matrix. It is square by virtue of there being the same number of equivalent grid points per cell as coefficients per cell. The coefficients of **R** can be produced readily by inserting the value of the scaling and wavelet coefficients at each equivalent grid point in the cell. An example of this matrix is the reconstruction of the E_x field for the r_{max}=0 case of (5), using the wavelets of Fig. 3 at the equivalent grid points of Fig. 4:

$$ \begin{bmatrix} \mathbf{E}_{1,1} \\ \mathbf{E}_{1,2} \\ \mathbf{E}_{2,1} \\ \mathbf{E}_{2,2} \end{bmatrix} = \begin{bmatrix} 1 & 1 & 1 & 1 \\ 1 & 1 & -1 & -1 \\ 1 & -1 & 1 & -1 \\ 1 & -1 & -1 & 1 \end{bmatrix} \begin{bmatrix} {}_{n}\mathbf{E}^{\mathbf{x},\varphi\varphi}_{\mathbf{i,j}} \\ {}_{n}\mathbf{E}^{\mathbf{x},\psi\varphi}_{\mathbf{i,j}} \\ {}_{n}\mathbf{E}^{\mathbf{x},\varphi\psi}_{\mathbf{i,j}} \\ {}_{n}\mathbf{E}^{\mathbf{x},\psi\psi}_{\mathbf{i,j}} \end{bmatrix} \tag{12} $$

IV. Intracell PEC Modeling

The MRTD method derived in the previous section contains a built-in adaptive resolution scheme in that the maximum level of wavelet resolution can be varied on a cell-by-cell basis. In addition, the wavelet resolution can be modified during simulation to allow for higher resolution as fields propagate through a cell. This technique allows relatively large low resolution cells to be used throughout the MRTD grid, and the resolution to be increased when needed. This time- and space-adaptive grid is very useful in that it enables efficient simulations, but is limited by the application of

PECs.

The PEC represents a boundary condition of zero electric field tangential to the conductor surface. The electric field coefficient update equation in MRTD (or FDTD) involves only the previous value of the coefficient (or field) and the values of the surrounding magnetic field coefficients of all resolution levels. In FDTD the PEC boundary condition can be applied at a single grid location by zeroing the electric field coefficient at that point. In MRTD, single equivalent grid points cannot be zeroed because their values are the sum of several scaling and wavelet coefficients. Setting these coefficients to zero would not only affect the desired point, but would also change the values of the fields on the surrounding equivalent grid points. This interaction between grid points is not consistent with Maxwell's equations.

This limitation has previously led to the restriction of having to zero all coefficients in a cell to represent a PEC boundary condition and necessitated the use of MRTD cells of the same size as fine features in the simulation, which limits the effectiveness of the MRTD adaptive grid. A method that allows individual equivalent grid points to be zeroed would enable the use of large MRTD cells throughout the simulation space, allowing the representation of complex details through the use of high resolution cells, while lower resolution cells are used elsewhere.

A technique that allows for individual equivalent grid points to be zeroed can be derived through the use of the reconstruction matrix. The matrix **R** in (11) transforms the wavelet coefficients to their equivalent grid points. The inverse of the matrix $\mathbf{R}^{-1}$, then, can be used to transform arbitrary field values into their wavelet decomposition (discrete wavelet transform [16]). The application of a PEC then becomes a three step process. First, the **R** matrix is used to transform the wavelet values into the field values at the equivalent grid points. Next, the field values that coincide with PEC locations are zeroed. Finally, the field values are transformed back to their wavelet coefficients using $\mathbf{R}^{-1}$ and the simulation continues. Using this method, any combination of equivalent grid points can be zeroed.

The wavelet decomposition matrix can be determined prior to simulation, therefore no matrix inversion is performed during simulation. In addition, the three step process described in the previous paragraph can be performed in one step, with one matrix multiplication. A PEC matrix, **P**, can be defined which directly transforms the wavelets from their non-PEC to PEC values. This matrix can be determined prior to simulation as,

$$\mathbf{P} = \mathbf{R}^{-1}\mathbf{R}' \tag{13}$$

In this equation **R'** is the standard reconstruction matrix, with the rows that correspond to the PEC field points set to zero.

For example, in r_{max}=0 MRTD, the **R** matrix is given in (12). If equivalent grid points (2,1) and (2,2) of Fig. 4 are to be zeroed,

$$\mathbf{R}' = \begin{bmatrix} \mathbf{1} & \mathbf{1} & \mathbf{1} & \mathbf{1} \\ \mathbf{1} & \mathbf{1} & \mathbf{-1} & \mathbf{-1} \\ \mathbf{0} & \mathbf{0} & \mathbf{0} & \mathbf{0} \\ \mathbf{0} & \mathbf{0} & \mathbf{0} & \mathbf{0} \end{bmatrix} \tag{14}$$

because, as shown in (12), the third and fourth rows of the reconstruction matrix give the fields at these points. In this case

$$\mathbf{R}^{-1} = \begin{bmatrix} \tfrac{1}{4} & \tfrac{1}{4} & \tfrac{1}{4} & \tfrac{1}{4} \\ \tfrac{1}{4} & \tfrac{1}{4} & -\tfrac{1}{4} & -\tfrac{1}{4} \\ \tfrac{1}{4} & -\tfrac{1}{4} & \tfrac{1}{4} & -\tfrac{1}{4} \\ \tfrac{1}{4} & -\tfrac{1}{4} & -\tfrac{1}{4} & \tfrac{1}{4} \end{bmatrix} \tag{15}$$

and, using (13),

$$\mathbf{P} = \begin{bmatrix} \tfrac{1}{2} & \tfrac{1}{2} & 0 & 0 \\ \tfrac{1}{2} & \tfrac{1}{2} & 0 & 0 \\ 0 & 0 & \tfrac{1}{2} & \tfrac{1}{2} \\ 0 & 0 & \tfrac{1}{2} & \tfrac{1}{2} \end{bmatrix} \tag{16}$$

It is clear that if no PEC is applied, **R'**=**R** and **P** is the identity matrix. Using the PEC matrix, **P**

$$_{\mathbf{n}}\mathbf{E}^{\mathbf{x}}_{\mathbf{i,j,PEC}} = \mathbf{P}\,{}_{\mathbf{n}}\mathbf{E}^{\mathbf{x}}_{\mathbf{i,j}} \tag{17}$$

If this matrix is used in the case of the previous example, the coefficients contained in $_{\mathbf{n}}\mathbf{E}^{\mathbf{x}}_{\mathbf{i,j,PEC}}$ will be different than those in $_{n}\mathbf{E}^{\mathbf{x}}_{\mathbf{i,j}}$; however they will reconstruct to the same values at all points in Fig. 4 except for (2,1) and (2,2), where they will reconstruct to 0. If the **P** matrices are determined prior to simulation, the application of PEC at arbitrary equivalent grid points becomes a matter of matrix multiplication in each cell that contains a PEC. A special case of this technique is presented in [17] as an FDTD/MRTD transform. The technique presented here is significantly extended because it can be applied to any arrangement of grid points, not just FDTD. This is necessary when used with space- and time-adaptive grids, and it provides the ability to use the wavelet/scaling representation of MRTD and modify the electromagnetic fields at specific points.

This technique has other direct applications to MRTD. The application of any condition that requires the modification of the field values at individual grid points can be performed using this approach. For example, an arbitrary value can be added to any equivalent grid point in order to simulate source conditions. Using this decomposition technique, the excitation can be finely shaped to match a desired mode.

The presented technique can be extended in two ways that merit special attention. First, the requirement that the permittivity and permeability of the material vary with the cell boundaries is not necessary for the derivation and was only added for ease of notation. Methods have been demonstrated [13,14] which allow these parameters to be varied continuously within a cell. These techniques are compatible with the subcell PEC modeling presented here, and when combined enable the use of composite cells that can contain

multiple material and PEC interfaces.

Finally, this technique can be applied to other wavelet bases. Using the same method, the fields in the MRTD scheme can be reconstructed. The fields at desired points can be explicitly modified, and then the fields in the entire grid can be transformed back to the wavelet domain. The effectiveness of this technique will be explored in future work for bases such as Daubechies and Battle-Lemarie. Using Haar wavelets for this technique is a particularly useful special case because the fields are constant over a discrete area and the reconstruction/decomposition operations take the form of matrix multiplications.

V. EXAMPLES

A. Solid Metal Wall – Discussion

The technique described in this paper can be used to apply the PEC boundary condition at any equivalent grid point in a structure. One aspect of this technique that may seem troublesome is that of a solid metal wall. If a computational space is intersected by a metal wall of one equivalent cell thickness, the space on either side of the PEC should be decoupled. However, the scaling function and some wavelets have non-zero value and extend across the PEC border. In this case the proposed technique does indeed decouple the computational domain. This can be demonstrated using (8).

For the purposes of this discussion, only the relationship between the H_z and E_y fields is considered. The previous value of the H_z field has no bearing on the coupling. It will be made clear that the technique decouples the E_x fields in the same way as the E_y, and therefore the E_x fields are neglected for this discussion. Finally, **U** is a non square matrix because it is multiplied by a column vector representing the coefficients of two neighboring E cells. After removing the time index and the H_z and E_x components from (8), and considering the two E_y cells needed for the update separately, the following results:

$$\mathbf{H}^{\mathbf{z}}_{\mathbf{i,j}} = -\frac{\Delta t}{\mu \Delta y}\left(\mathbf{U}_1\mathbf{E}^{\mathbf{y}}_{\mathbf{i,j}} + \mathbf{U}_2\mathbf{E}^{\mathbf{y}}_{\mathbf{i+1,j}}\right) \tag{18}$$

By considering the E_y fields separately, the **U** matrix has been split into two separate matrices, $\mathbf{U_1}$ and $\mathbf{U_2}$, which are the portions of the original **U** matrix related to each of the individual $\mathbf{E_y}$ fields. The coefficients of the E field after the PEC has been applied can be determined as in (17) by multiplying the E fields with **P**.

$$\mathbf{RH}^{\mathbf{z}}_{\mathbf{i,j}} = \mathbf{H}^{\mathbf{z}}_{\mathbf{i,j,field}} = -\frac{\Delta t}{\mu \Delta y}\left(\mathbf{RU}_1\mathbf{P}_1\mathbf{E}^{\mathbf{y}}_{\mathbf{i,j}} + \mathbf{RU}_2\mathbf{P}_2\mathbf{E}^{\mathbf{y}}_{\mathbf{i+1,j}}\right) \tag{19}$$

A different **P** is used for each E field, representing different PEC conditions within each cell. If both sides of the equation are then left multiplied with the reconstruction matrix, the equation gives the H field values based on the E components after the PEC modification has been applied,

$$\mathbf{RH}^{\mathbf{z}}_{\mathbf{i,j}} = \mathbf{H}^{\mathbf{z}}_{\mathbf{i,j,field}} = -\frac{\Delta t}{\mu \Delta y}\left(\mathbf{RU}_1\mathbf{P}_1\mathbf{E}^{\mathbf{y}}_{\mathbf{i,j}} + \mathbf{RU}_2\mathbf{P}_2\mathbf{E}^{\mathbf{y}}_{\mathbf{i+1,j}}\right) \tag{19}$$

or equivalently

$$\mathbf{RH}^{\mathbf{z}}_{\mathbf{i,j}} = \mathbf{H}^{\mathbf{z}}_{\mathbf{i,j,field}} = -\frac{\Delta t}{\mu \Delta y}\left(\mathbf{RU}_1\mathbf{P}_1\mathbf{E}^{\mathbf{y}}_{\mathbf{i,j}} + \mathbf{RU}_2\mathbf{P}_2\mathbf{E}^{\mathbf{y}}_{\mathbf{i+1,j}}\right) \tag{20}$$

Replacing $\mathbf{RE}^{\mathbf{y}}_{\mathbf{i,j}}$ with $\mathbf{E}^{\mathbf{y}}_{\mathbf{i,j,field}}$ yields

$$\mathbf{H}^{\mathbf{z}}_{\mathbf{i,j,field}} = -\frac{\Delta t}{\mu \Delta y}\left(\mathbf{RU}_1\mathbf{P}_1\mathbf{R}^{-1}\mathbf{E}^{\mathbf{y}}_{\mathbf{i,j,fields}} + \mathbf{RU}_2\mathbf{P}_2\mathbf{R}^{-1}\mathbf{E}^{\mathbf{y}}_{\mathbf{i+1,j,fields}}\right) \tag{21}$$

The matrices of (21) can be combined to give a single U' matrix,

$$\mathbf{H}^{\mathbf{z}}_{\mathbf{i,j,field}} = -\frac{\Delta t}{\mu \Delta y}\left(\mathbf{U'}_1\,\mathbf{E}^{\mathbf{y}}_{\mathbf{i,j,field}} + \mathbf{U'}_2\,\mathbf{E}^{\mathbf{y}}_{\mathbf{i+1,j,field}}\right) \tag{22}$$

$$\mathbf{U'} = \mathbf{RUPR}^{-1} \tag{23}$$

To show that the fields on either side of the PEC are decoupled, it remains to show that rows of the **U** matrix that correspond to H fields on opposite sides of the PEC wall are not related.

The example of a y directed PEC intersecting 1 column of equivalent E_y grid points in a simulator with r_{max}=0 is presented. The cells that make up the H_z update in this case are presented in Fig. 6. The PEC is applied to the rightmost equivalent grid points of the first E_y cell. This metal wall splits the H_z cell in two and decouples the fields on either side. The **R** matrix for this case is given in (12), $\mathbf{R^{-1}}$ is given in (15). For the left E_y cell in Fig. 6, **P** is given in (16). For the right E_y cell, **P** is the identity matrix. The **U** matrices are given in (9), separated they are:

$$\mathbf{U}_1 = \begin{bmatrix} -1 & -1 & 0 & 0 \\ 1 & -3 & 0 & 0 \\ 0 & 0 & -1 & -1 \\ 0 & 0 & 1 & -3 \end{bmatrix} \tag{24}$$

$$\mathbf{U}_2 = \begin{bmatrix} 1 & 1 & 0 & 0 \\ -1 & -1 & 0 & 0 \\ 0 & 0 & 1 & 1 \\ 0 & 0 & -1 & -1 \end{bmatrix} \tag{25}$$

In this case, using (23),

$$\mathbf{U'}_1 = \begin{bmatrix} -2 & 0 & 0 & 0 \\ 0 & -2 & 0 & 0 \\ 0 & 0 & 0 & 0 \\ 0 & 0 & 0 & 0 \end{bmatrix} \tag{26}$$

$$\mathbf{U'}_2 = \begin{bmatrix} 0 & 0 & 0 & 0 \\ 0 & 0 & 0 & 0 \\ 2 & 0 & 0 & 0 \\ 0 & 2 & 0 & 0 \end{bmatrix} \tag{27}$$

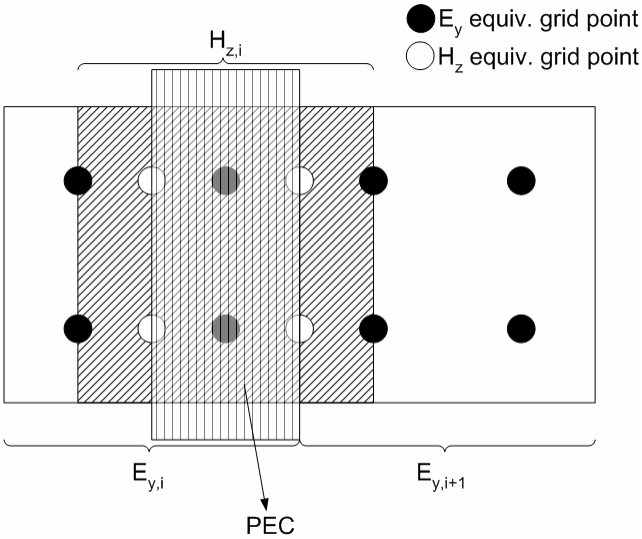

Fig. 6 Cells needed for Hz update, Ey fields intersected by PEC

From these matrices it can be seen that the H_z fields depend only on the fields directly adjacent to them. The left two H_z fields (represented by the top two rows of the matrix) only depend on the leftmost fields of the first E_y cell (represented by the first two columns of the matrix). Likewise, the rightmost H_z fields depend only on the leftmost fields of the second E_y cell. The fields covered by the PEC have no contribution. These matrices represent update equations equivalent to FDTD. In an FDTD matrix, magnitudes of the coefficients in (26) and (27) would be one, instead of two as seen here. The discrepancy comes from the fact that the distance between two equivalent grid points is not Δx or Δy in this case, but $\Delta x/2$ or $\Delta y/2$. As the H_z fields only depend on E_y fields on their side of the PEC, the fields are indeed decoupled.

B. Solid Metal Wall – Simulation Example

This property of subcell modeling can also be directly demonstrated by simulation. A 2D MRTD simulator using the technique described above was used to model a parallel plate waveguide. The waveguide, shown in Fig. 7, has a width of 7.5cm; two MRTD cells with r_{max}=2 (64 points/cell) were used to model this width. A metal wall with a width of one equivalent grid point (1/8 of the cell size), is located four equivalent grid points from the cell edge and splits the waveguide in two. A TEM excitation is simulated by exciting the electric fields normal to the waveguide wall. A Gaussian (in time) excitation is placed on both sides of (although, not equidistant from) the metal wall. If the wall truly subdivides the space, complete reflection will occur on either side of the wall. If not, some of the excited wave from either side should be transmitted through the wall.

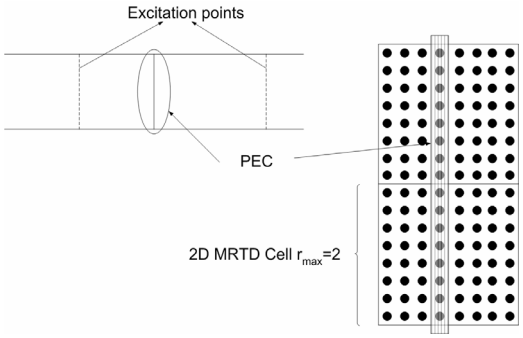

Fig. 7 Metal wall intersecting parallel plate waveguide

As expected, total reflection results, as can be observed in Fig. 8. The probed field is located adjacent to the excitation point on both sides. As these excitations are applied at different distances from the wall, the reflection is observed at different times. The reflected pulse in each case is equal to the negative of the incident pulse, indicating complete reflection from a PEC surface.

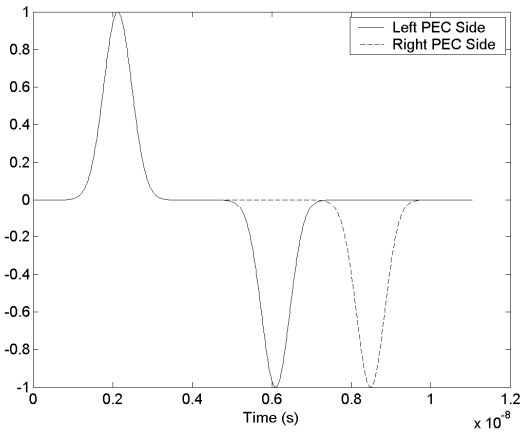

Fig. 8 Time domain results for excitation on either side of PEC

C. PEC Screen

A more concrete example of the applicability of this method can be presented using a PEC screen embedded into a parallel plate waveguide. This structure is simulated in two dimensions and is presented in Fig. 9. The screen used in this case is made up of small metal structures that cut through the waveguide. This geometry is similar to EBG structures consisting of vias which are used in many applications. This arrangement is chosen because it contains small and closely spaced metallic elements. The structure is simulated in a fixed grid FDTD, fixed grid MRTD, and a variable grid MRTD. The fixed grid MRTD method used in this case has an identical equivalent grid (the locations of the equivalent grid points) as the FDTD simulation. In this way the MRTD and FDTD simulations can be compared. The advantage of using this method, however, comes from the ability to vary resolution in the MRTD case. The variable gridded MRTD uses high resolution in the area of the PEC screen, and low resolution cells elsewhere.

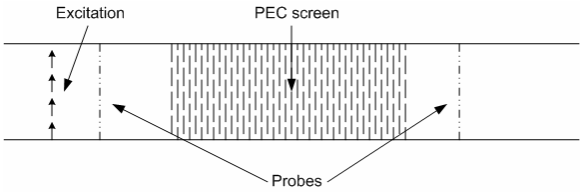

Fig. 9 Parallel plate waveguide with PEC screen

A portion of the grid used in the MRTD simulations is presented in Fig. 10. This figure shows the interface between the open parallel plate waveguide and the screen area. The MRTD simulations both use a maximum resolution level of two in the screen area. This corresponds to 64 equivalent grid points per MRTD cell. Overall, six cells are shown, with only the first four rows of the screen shown. Two rows of the PEC screen are in each cell; the screen consists of twenty of these cells repeated. The fixed grid MRTD uses the same resolution in the entire simulation grid. The FDTD simulation has a grid that overlaps the equivalent grid points. In the case of the variably gridded MRTD simulation, the resolution two cells away from the screen is reduced by one order. In this simulation, that corresponds to 48 less cells, or a 75% reduction in the number of points to update in the area surrounding the PEC screen. Overall, this results in a 67% reduction in coefficients to update. The total grid size is 200x2 MRTD cells, or, in the FDTD case 1600x16 (which is equal to the number of equivalent grid points in the fixed MRTD case). The variable grid MRTD simulation has 8512 equivalent grid points (or coefficients) compared to 25,600 for the fixed grid MRTD or equivalent FDTD case.

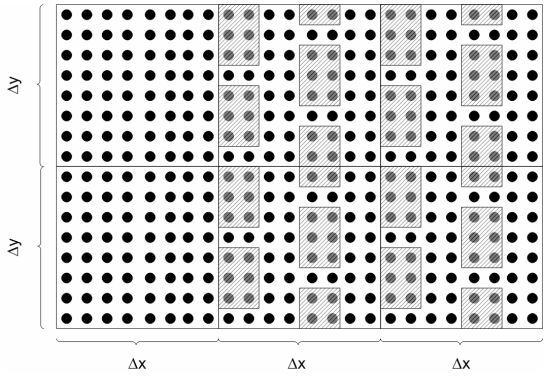

Fig. 10 Cells in screen area for parallel plate waveguide with PEC screen

Time-domain simulation results for all three simulation methods are presented in Fig. 11. In these simulations the response is due to a Gaussian waveform (TEM mode) incident on the screen. These results show the magnitude of the voltage between the waveguide plates at the output of the screen. The location of the probe is chosen to be the same for all simulations. From Fig. 11 it is clear that the results for all three cases are very similar, Figs. 12 and 13 quantify this similarity.

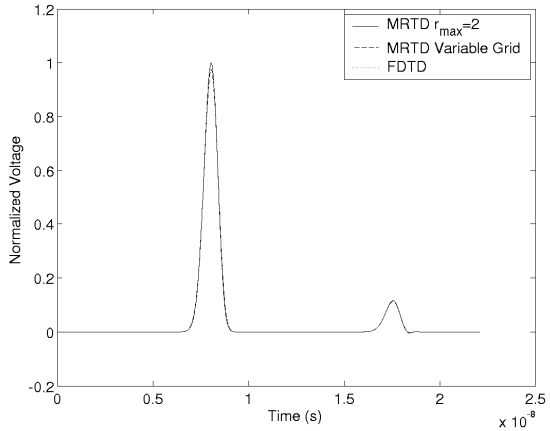

Fig. 11 Time domain output voltage for parallel plate waveguide with PEC screen, FDTD/MRTD/MRTD variable grid comparison

Fig. 12 shows the difference between the FDTD and MRTD fixed grid simulation, normalized to the peak voltage value. As the grids for these two cases overlap, it is expected that the results should be very close. The difference between the cases is on the order of 10^{-14}. For the simulation environment used here, these values indicate numerical roundoff error, showing that the methods are in fact identical.

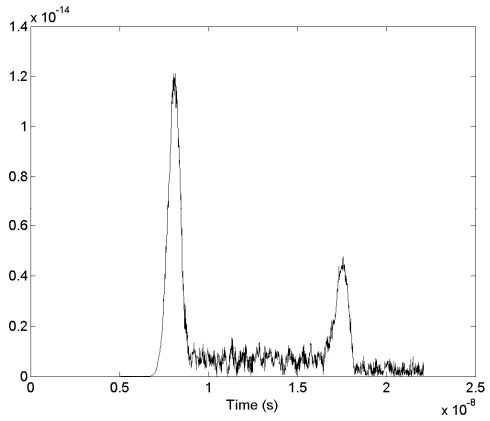

Fig. 12 Magnitude of difference between MRTD and FDTD parallel plate waveguide with PEC screen output voltage (normalized to maximum voltage)

Fig. 13 shows the difference between the variably gridded MRTD and the fixed grid MRTD. As expected, there are small, but significant, differences between the output voltage. This is due to the differences in resolution between the simulations. The higher resolution fixed-grid simulation is expected to be more accurate, at the expense of simulation time. In this case the 75% reduction in grid points in the area surrounding the screen translates directly to a 75% reduction in computation time (and memory use) in these areas for the variable grid. This demonstrates how the method presented in this paper can be used to gain the advantages of variable resolution MRTD while simulating finely detailed structures.

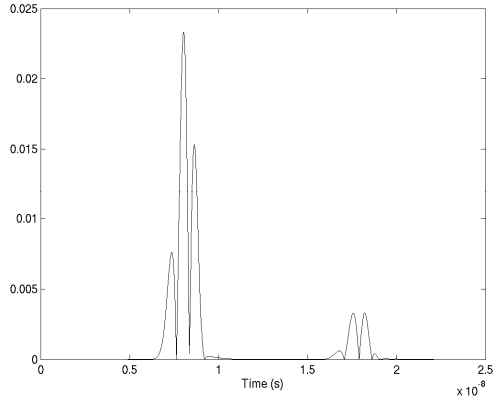

Fig. 13 Magnitude of difference between MRTD and MRTD variable grid parallel plate waveguide with PEC screen output voltage (normalized to maximum voltage)

D. Microstrip Patch Antenna

As a final example a microstrip patch antenna was simulated using a 3D MRTD code that implemented the composite cell method. The patch antenna is designed for 31GHz operation, and is placed on a 200μm thick polyamide film with ε_r=3.2. A diagram of the antenna is presented in Fig. 14. The inset on the antenna matches it to the 50Ω feed line.

For this structure the subcell grid is primarily used to model the direction normal to the surface of the antenna. For any PEC structures in MRTD, the subcell grid must be used if they are one equivalent cell in thickness (the most common condition for printed devices). In addition, this structure uses the subcell grid to model the edges of the antenna, although it would be relatively easy to find a grid that matched the structure without the subcell modeling.

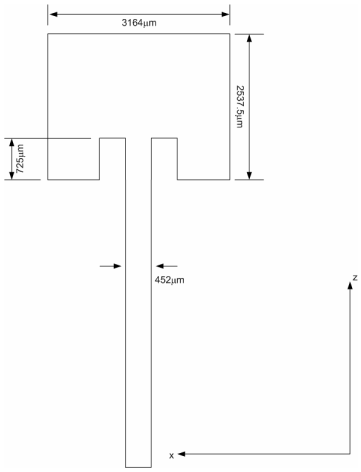

Fig. 14 Microstrip patch antenna

The MRTD grid that is used to model the structure is 40 x 7 x 92 including three cells of UPML absorber in each direction (only on the top in the direction normal to the printed structure). For each direction, r_{max}=1. This places four equivalent grid points in each direction for a total of 64 equivalent grid points per cell. One cell is used to model the substrate thickness, for a total of four equivalent grid points representing the substrate. The total number of MRTD cells is 6440. An equivalent simulation was run in FDTD, with the MRTD equivalent grid points and FDTD grid points overlapped. In this case the FDTD grid used 412,160 cells.

S_{11} for both the MRTD and FDTD simulation is presented in Fig. 15. In this figure the MRTD results and FDTD results show a slightly different resonant frequency. In Fig. 16, time domain results are shown for the simulations, and in this figure a small discrepancy between the two simulations is also observed.

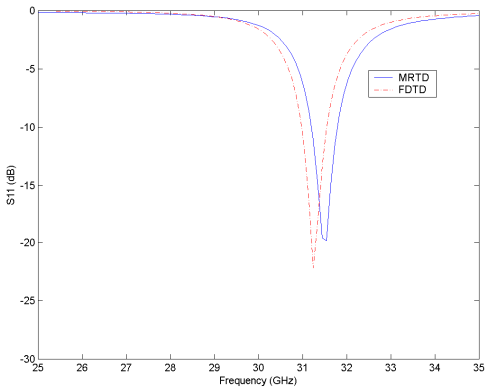

Fig. 15 S_{11} of patch antenna, MRTD/FDTD comparison

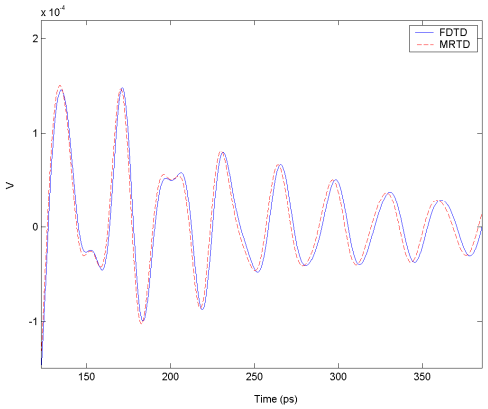

Fig. 16 Close-up of differences between MRTD/FDTD, time domain

The differences between the FDTD and MRTD simulations are due to the method used to simulate dielectric discontinuities. In the FDTD simulation, the dielectric constant used at the interface between the two materials is the average of the surrounding values. In the MRTD case, however, the interface is simulated by a separate update equation that solves for the electric field components from the electric flux field components [7]. The differences between these methods cause the disagreement in the output.

If the material above and below the antenna is homogeneous, the FDTD and MRTD results are identical. S_{11} for this case is presented in Fig. 17, where the above case is simulated with the modification that ε_r is equal above and below the antenna.

In these comparison cases, the same grid was used for both

the MRTD and FDTD cases. However, this is not a very efficient use of the MRTD composite-cell method. Another MRTD simulation was performed where the resolution of the MRTD grid was fixed at -1 surrounding the antenna (3 MRTD cells from the antenna boundary). In this case, the number of equivalent grid points required to simulate the antenna was 34% less than the constant resolution case, while the error in the time domain response at the input of the antenna was less than 1%. The number of equivalent grid points is directly proportional to the computational load, and, as expected, a 34% reduction in computation time was also observed.

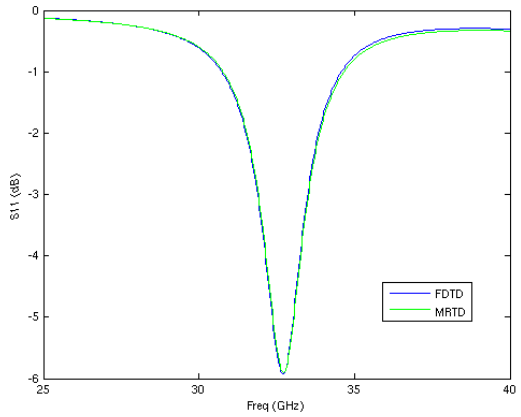

Fig. 17 FDTD/MRTD comparison, constant ε_r

VI. Conclusion

The technique presented in this paper enables the modeling of arbitrarily shaped PEC structures within Haar MRTD cells. Three examples were given that demonstrate the effectiveness of the technique and how it can be made equivalent to the established FDTD method. This technique dramatically extends the power of the MRTD method because it allows the adaptive grid to be used on finely detailed structures while using large MRTD cells. In addition, fewer overall equivalent grid points are required for the modeling of any structure. The ability to use large MRTD cells to model fine details makes it possible to simulate complex 3D structures such as MEMS, EBG, and complex MMIC circuits. Through this technique, the large predicted efficiencies of the MRTD method can be achieved for complex antenna structures including fine metal details.

References

[1] M. Hill, R. Ziolkowski, and J. Papapolymerou, "A high-Q reconfigurable planar EBG cavity resonator," *IEEE Microwave and Wireless Comp. Letters*, vol. 11, no. 6, pp. 255-257, June 2001.

[2] Kildal, P.S., "Artifically soft and hard surfaces in electromagnetics," *IEEE Trans. Antennas and Prop.* vol. 38, no. 10, pp. pp. 1537-1544, Oct. 1990.

[3] R. Ziolkowski, and A. Kipple, "Application of double negative materials to increase the power radiated by electrically small antennas," *IEEE Trans. on Antennas and Prop.*, vol. 51, no. 10, pp. 2626-2640, Oct. 2003K. S. Yee, "Numerical solution of initial boundary value problems involving Maxwell's equations in isotropic media", *IEEE Trans. Antennas Propagat*., vol.AP-14, pp.302-307, Mar. 1966.

[4] K. S. Yee, "Numerical solution of initial boundary value problems involving Maxwell's equations in isotropic media", IEEE Trans. Antennas Propagat., vol.AP-14, pp.302-307, Mar. 1966.

[5] S.D. Gedney and F. Lansing "Explicit time-domain solution of Maxwell's equation using nonorthogonal and ununstructured grids," ch 11 in *Computational Electrodynamics: The Finite Difference Time Domain Method*, A. Taflove, Ed. Norwood, MA: Artech House, 1995.

[6] I. S. Kim, W. J. R. Hoefer, "A local mesh refinement algorithm for the time domain finite difference method using Maxwell's curl equations," *IEEE Trans. Microwave Theory Tech.*, vol. 38, no. 6, pp.812-815, June 1990.

[7] M. Krumpholz, L. P. B. Katehi, "New time domain schemes based on multiresolution analysis", *IEEE Trans. Microwave Theory Tech.*, vol.44, pp.555-561, Apr. 1996

[8] E.Tentzeris, R.Robertson, J.Harvey and L.P.B.Katehi, "Stability and Dispersion Analysis of Battle-Lemarie Based MRTD Schemes", *IEEE Trans Microwave Theory and Tech.*, vol.47, No.7, pp.1004-1013, July 1999

[9] T. Dogaru and L. Carin, "Scattering analysis by the multiresolution time-domain method using compactly supported wavelet systems," IEEE Trans. Microwave Theory Tech, vol. 50, no. 7, pp.1752-1760 July 2002.

[10] Y. V. Tretiakov and G. W. Pan, "On Daubechies wavelet based time domain scheme," *Proc. IEEE Symposium Antennas Prop.*, pp. 810-813, Boston, 2001.

[11] T. Dogaru and L. Carin, "Multiresoultion time-domain using CDF biorthagonal wavelets," *IEEE Trans. Microwave Theory Tech*, vol. 49, no. 5, pp.902-912, May 2001.

[12] N. Bushyager, J. Papolymerou, and M. Tentzeris, "A composite-cell multiresolution time-domain technique for design of electromagnetic band-gap and via-array structures," *Proc. 2003 IEEE MTTS*, vol. 3, pp. 2081-2084, June 2003.

[13] E. M. Tentzeris, A. Cangellaris, L. P. B. Katehi, and J. Harvey, "Multiresolution Time-Domain (MRTD) Adaptive Schemes Using Arbitrary Resolutions of Wavelets," *IEEE Trans. Microwave Theory Tech*, vol. 50, no. 2, pp 501-516, Feb. 2002.

[14] T. Dogaru and L. Carin, "Application of Haar-wavelet-based multiresolution time-domain schemes to electromagnetic scattering problems," *IEEE Trans. Antennas Prop.*, vol. 50, no. 6, pp.774-784, June 2002.

[15] C. Sarris and L. P. B. Katehi, "Fundamental gridding-related dispersion effects in multiresolution time-domain schemes," *IEEE Trans. Microwave Theory Tech*, vol. 49, no. 12, pp 2248-2257, Dec. 2001.

[16] I. Daubechies, Ten lectures on wavelets, Philadelphia: SIAM, 1992.

[17] G. Carat, R. Gillard, J. Citerne, and J. Wiart, "An efficient analysis of planar microwave circuits using a DWT-based Haar MRTD scheme," *IEEE Trans. Microwave Theory Tech.,* vol. 48, no. 12, pp. 2261-2270, Dec. 2000.